




# Microstructure, mechanical properties, and texture evolution of Mg–Zn–Y–Zr alloy fabricated by hot extrusion–shearing process

Shuai Dai<sup>1</sup>, Feng Wang<sup>1,\*</sup> , Zhi Wang<sup>1</sup>, Zheng Liu<sup>1</sup>, and Pingli Mao<sup>1</sup>

<sup>1</sup> School of Materials Science and Engineering, Shenyang University of Technology, Shenyang 110870, People's Republic of China

Received: 21 April 2019

Accepted: 20 August 2019

Published online:  
27 August 2019

© Springer Science+Business  
Media, LLC, part of Springer  
Nature 2019

## ABSTRACT

In this study, ultrafine-grained Mg–Zn–Y–Zr alloys were obtained via a novel extrusion–shearing (ES) deformation process, which combined initial forward extrusion with subsequent shearing. The experimental results showed that the composition of the main phase was converted from the  $\alpha$ -Mg, I ( $\text{Mg}_3\text{Zn}_6\text{Y}$ ), and W ( $\text{Mg}_3\text{Zn}_3\text{Y}_2$ ) phases to the  $\alpha$ -Mg and W phases as the Zn/Y mass ratio of the as-cast alloys decreased from 4 to 0.67. Needle-shaped  $\text{YZn}_5$  and micron-sized  $\text{Mg}_7\text{Zn}_3$  phases were also observed in the as-homogenized Mg–4Zn–1Y–0.6Zr and Mg–3Zn–2Y–0.6Zr alloys. The quantitative electron backscatter diffraction results demonstrated that the dynamic recrystallization (DRX) and the growth of fine DRX grains had a strong dependence on the equivalent strain and increased temperature caused by the die corner. The abundance of W precipitates resulted in the gradual evolution of the sub-grains into fresh DRX grains for the ES alloy III. Additionally, reduced strength anisotropies were related to the decreased pole density caused by the increasing addition of Y; a weakened basal texture with a rare-earth texture component was also achieved at 3 wt% of Y addition. Finally, the influences of the grain size and basal texture on the ductility and strength of the ES alloys were systematically investigated.

## Introduction

Magnesium (Mg) alloys have a significant potential for industrial applications owing to their high specific strength, specific stiffness, and good casting properties [1, 2]. Grain-boundary strengthening plays an important role in the mechanical properties of extruded Mg alloys. They have a higher  $k_y$  slope value in the Hall–Petch formula compared with other

alloys, and ultrafine-grained alloys with superior mechanical properties can be obtained via severe plastic deformation (SPD). Hence, Mg alloys are desirable candidates for commercial applications [3, 4]. Presently, among the SPD methods, equal channel angular pressing (ECAP) is considered one of the most promising for Mg alloys [5]. The strong texture developed during the traditional extrusion process can slightly enhance the tensile strength

Address correspondence to E-mail: wf9709@126.com

under tensile loading parallel to the extrusion direction (ED), while also adversely affecting the anisotropic strength of the extruded alloy. Moreover, Chino et al. [6] observed that  $\{10\bar{1}1\}$  contraction twins and  $\{10\bar{1}1\}$ – $\{10\bar{1}2\}$  double twins more easily occurred in coarse non-DRX grains than in fine DRX grains, resulting in a decrease in the ductility. However, during ECAP, activation of shear forces in the die corner can further promote the DRX by rotating coarse non-DRX grains to obtain ultrafine equiaxial grains while weakening the basal texture of the DRX grains [7]. This can result in an improvement in the strength and plasticity of the ECAP alloys, as well as a decrease in yield asymmetry [8]. Janeček et al. [9] previously developed an AZ31 alloy with an average grain size of  $\sim 1 \mu\text{m}$  and a weakened basal texture using multi-pass ECAP. Different microstructures are achieved by altering the extrusion–shearing path, which can be ascribed to the uneven distribution of the equivalent strain at the die corner [10]. Undesirably, the von Mises criterion accounts for the difficult formability of the investigated sample via the multi-pass ECAP process.

Aside from the proposed ECAP method, Mg–Zn–RE system alloys have recently attracted considerable interest, using REs such as Y [11], Gd [12], Ce [13], Nd [14], and Dy [15]. Based on lattice matching, the addition of Y can significantly increase the effect of grain refinement on the as-cast alloys due to the heterogeneous nucleation sites formed because both Y and Mg are hcp structures with nearly similar lattice parameters. The reduced grain size in the billet results in pronounced grain refinement of the extruded alloy owing to an increase in the proportion of grain boundaries that can act as DRX nucleation sites [16]. As a result, the addition of RE-alloying elements is also a promising approach for grain refinement and texture weakening of the extruded alloys. Several phase compositions can be generated within the Mg–Zn–RE system alloys by adjusting different Zn/RE mass ratios. As the Zn/RE mass ratio increased from 0.27 to 1.4, the corresponding phase composition changes from the W and long-period stacking-ordered (LPSO) phases to W and I phases [17]. However, the low diffusivity of Zn atoms leads to a poor LPSO phase formation at low Zn contents. The existence of large particles distributed in the  $\alpha$ -Mg matrix can cause a strain large enough to result in DRX in the surrounding region [18]. Park et al. [19]

reported that the size and distribution of particles in a billet could significantly influence the refinement of the grain structure via the particle-stimulated nucleation (PSN) mechanism during hot deformation. Yin et al. [20] and Xu et al. [21] also demonstrated the important role of both the I and LPSO phases for DRX because of the superior thermal stability of the Mg alloys. The expected weak atomic bonding between the W phase and  $\alpha$ -Mg matrix primarily accounts for the W phase-containing alloys having relatively poor mechanical properties. In addition, nano-sized particles are formed via the precipitation of phases with poor stability dissolved in the  $\alpha$ -Mg matrix and the underlying precipitation effect may exist in the W phase. This in turn suppresses the growth of fine DRX grains by inhibiting the migration of grain boundaries during hot deformation, which is essential for the occurrence of DRX [22]. Oh-ishi et al. [23] also confirmed uniformly dispersed precipitates occurred within the original pinned grain dislocations, and the sub-grain structure ultimately evolved into DRX grains. The homogenization treatment (T4) is commonly used to enhance the precipitation effect during hot deformation. Bai et al. [24] completed similar work and indicated that T4 treatment prior to extruding the Mg–8Sn–4Zn–2Al alloys resulted in finer grain sizes, more homogenous microstructures, and weaker basal textures than those of the as-cast alloys. Zhang et al. [25] proposed a novel plastic deformation method that included the initial forward extrusion and subsequent shearing process (ES) that could result in an increase in the volume fraction of the DRX grains owing to the improvement in the equivalent strain.

In this work, a novel steel die with an extrusion ratio of 11.56 that combines an initial forward extrusion and subsequent shearing process is proposed. The internal angles between the two channels and an external angle were designed as  $90^\circ$  and  $0^\circ$ , respectively, with the aim of obtaining samples that avoid cracking under large equivalent strain [26]. The purpose of the present work was to understand the effect of the equivalent strain at the die corner and the different phase compositions obtained via changing the Zn/Y mass ratios on the microstructure, the mechanical properties, and the texture evolution of Mg–Zn–Y–Zr alloys. The strengthening mechanism was also discussed for the application of ES Mg–Zn–Y–Zr alloys.

## Experimental procedure

The as-cast Mg–4Zn–1Y–0.6Zr, Mg–3Zn–2Y–0.6Zr, and Mg–2Zn–3Y–0.6Zr alloys were prepared using high-purity (99.95%) Mg and Zn, Mg–25Y, and Mg–30Zr (wt %) master alloys. First, the pure Mg was melted at 700 °C in an electric resistance furnace under a protective gas mixture of 99.5% N<sub>2</sub> and 0.5% SF<sub>6</sub> (volume fraction). The Zn, Mg–25Y, and Mg–30Zr master alloys were added into the pure Mg melt after ~ 1.5 h, and the temperature was increased to 720 °C. The temperature was then maintained at 720 °C for 30 min to ensure that the alloying elements were completely dissolved. Subsequently, the melts were cooled to 700 °C and poured into a preheated metal mold ( $\Phi$  75 × 75 mm). Inductively coupled plasma mass spectrometry (ICP-AES) was then used to confirm the chemical compositions of the as-cast billets, and the corresponding results are presented in Table 1. Billets with a dimension of  $\Phi$  68 × 68 mm were machined from the ingot and homogenized at 400 °C for 25 h (T4), and water quenching was then used to obtain a supersaturated solid solution favorable to subsequent plastic deformation. The ingots were extruded to form a bar of 20 mm in diameter at 400 °C at an extrusion ratio of 11.56 and a die-exit speed of 40 mm/min. The detailed schematic illustrations of the ES die and sample are presented in Fig. 1a, b.

The as-cast and as-homogenized samples for microstructure observation were polished and etched with a 4% (volume fraction) nitrate alcohol solution, while the as-extruded samples were etched with glacial acetic acid containing 40 ml alcohol, 5 ml acetic acid, 3 g picric acid, and 5 ml distilled water. The microstructural evolution and phase analysis were investigated using a Zeiss Axio Observer A1 optical microscope (OM), Hitachi S-3400N scanning electron microscope (SEM) equipped with an energy-dispersive spectrometer (EDS), D/max III A X-ray diffractometer (XRD), and a JEM-2100 transmission

**Table 1** Actual chemical composition of alloys (mass fraction, %)

Alloy code	Alloy	Zn	Y	Zr	Mg
I	Mg–4Zn–1Y–0.6Zr	4.10	0.96	0.63	Bal.
II	Mg–3Zn–2Y–0.6Zr	2.95	1.93	0.60	Bal.
III	Mg–2Zn–3Y–0.6Zr	2.05	3.02	0.58	Bal.

electron microscope (TEM) operating at 200 kV. For TEM imaging, disk-shaped specimens with a thickness of 50  $\mu$ m and a diameter of 3 mm were fabricated via the metallographic technique. Then, the disk-shaped specimens were placed in a 3.5 kV Gatan 691 ion beam at 4° until a pinhole appeared near the center. Electron backscattered diffraction (EBSD) analysis was carried out on a Gemini SEM 300 equipped with an HKL–EBSD system operating at 15 kV with a step size of 0.2  $\mu$ m. The EBSD samples were mechanically and electrochemically polished in an electrolyte composed of 10% perchloric acid and 90% ethanol at 10 V and – 30 °C for 90 s. The samples for the tensile and compression tests had a gauge length of 10 mm and were obtained from the forming area in the ES bar via an electric spark machine. Single-axis tensile and compression tests were performed at ambient temperature using a WDW-100 universal testing machine at an initial strain rate of 10<sup>–3</sup> s<sup>–1</sup> with a loading direction parallel to ED.

## Results and discussion

### Microstructural characteristics of as-cast and as-homogenized alloys

Figure 2 shows the SEM images of the as-cast alloys. According to the EDS elemental analysis, the fine elongated particles distributed along the grain boundaries can be identified as the I phases, while the herringbone and lamellar-shaped particles are the W phases. Normally, the I phase is desirable as the underlying reinforcing phase of the Mg alloy because of its high thermal stability. The lamellar spacing of the W phase gradually decreased with decreasing Zn/Y mass ratios (Fig. 2d–f). Previous literature indicated that the decreased amount of Zn mainly accounted for the strong suppression of the lamellar W phase growth [27]. Long-period stacking-ordered (LPSO) phase is commonly observed in the Mg–Zn–RE alloy systems with a Zn/RE mass ratio of 0.67 [17]; hence, the low diffusion rate of the Zn atoms may demonstrate the inverse if insufficient Zn is present. A low amount of Zn<sub>3</sub>Zr<sub>2</sub> phases are coincidentally observed in alloy I (Fig. 2 d), as well as the other investigated alloys. The formation of the Zn<sub>3</sub>Zr<sub>2</sub> phase can be attributed to an inappropriate melting or a slow cooling rate during the casting process [28]. Diffraction peaks corresponding to the different

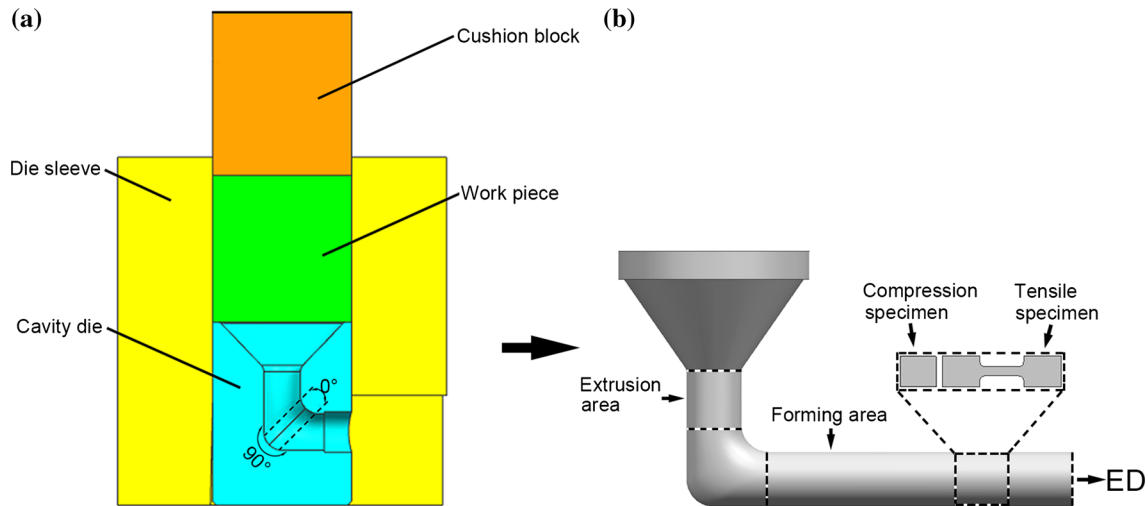


**Figure 1** Schematic illustration of **a** ES die and **b** ES sample model.

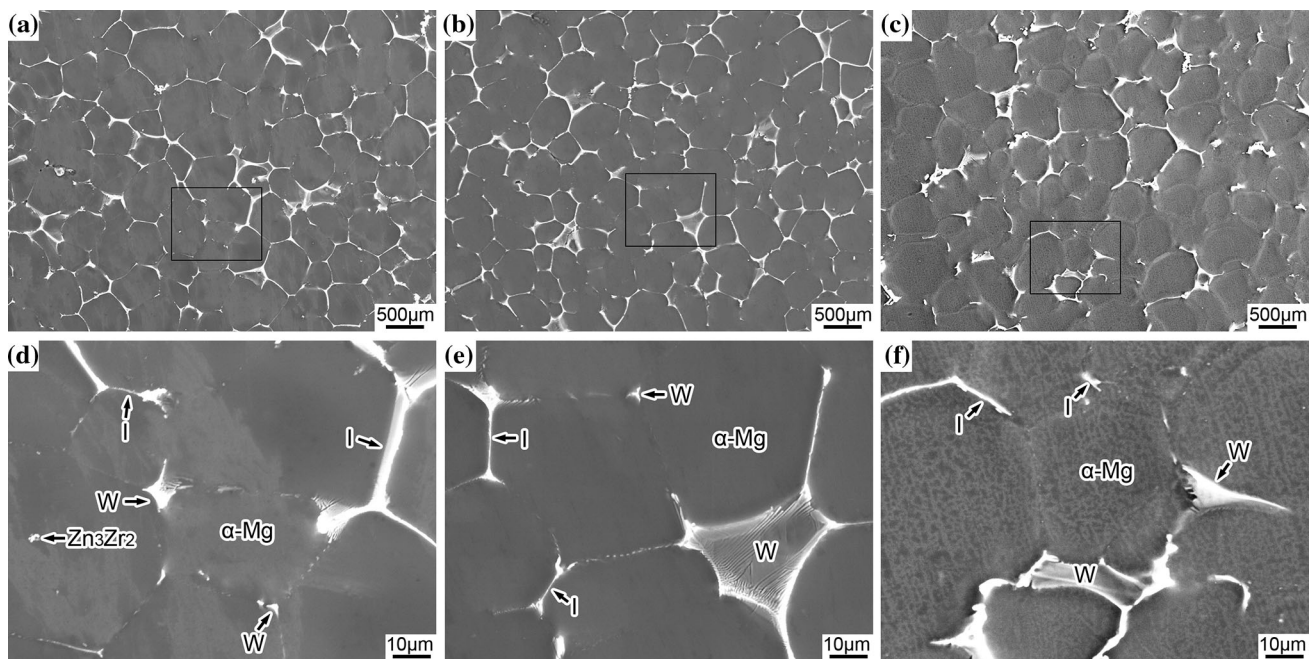


**Figure 2** Representative SEM microstructures of as-cast alloys: **a–c** low-magnification and **d–f** magnified images for the alloy (I–III), respectively.

phases are also observed from XRD analysis (Fig. 4a), except for the  $Zn_3Zr_2$  phase due to its low content. The diffraction peak intensities clearly demonstrate that the amount of I phases gradually decreased as the Zn/Y mass ratio increased, while the amount of the W phases increased.

SEM images of the as-homogenized alloys are shown in Fig. 3. After homogenization, the semi-continuous I phases along the grain boundaries change into a fully continuous morphology of alloy I

(Fig. 3a, d). The I phase can even grow in a faceted manner perpendicular to the  $\alpha$ -Mg matrix under heat treatment at 400 °C [29]. A major portion of the W phases fully dissolve in the  $\alpha$ -Mg matrix, and the residual W phases are dominant in alloy III (Fig. 3c, f). Because a eutectoid transformation of the W phase to the  $\alpha$ -Mg and  $YZn_5$  phases occurs after a long heat treatment, it is not surprising that numerous needle-shaped  $YZn_5$  phases are observed at grains in the interiors of alloy I (Fig. 3d). As for alloy II, the

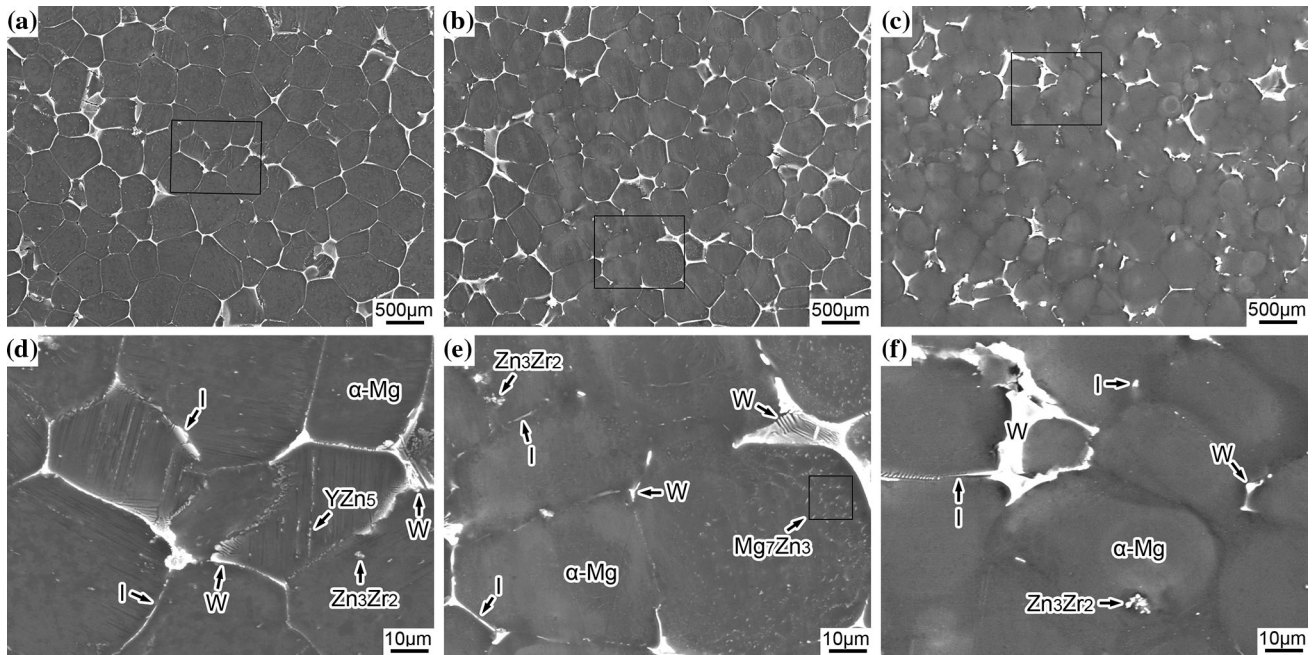


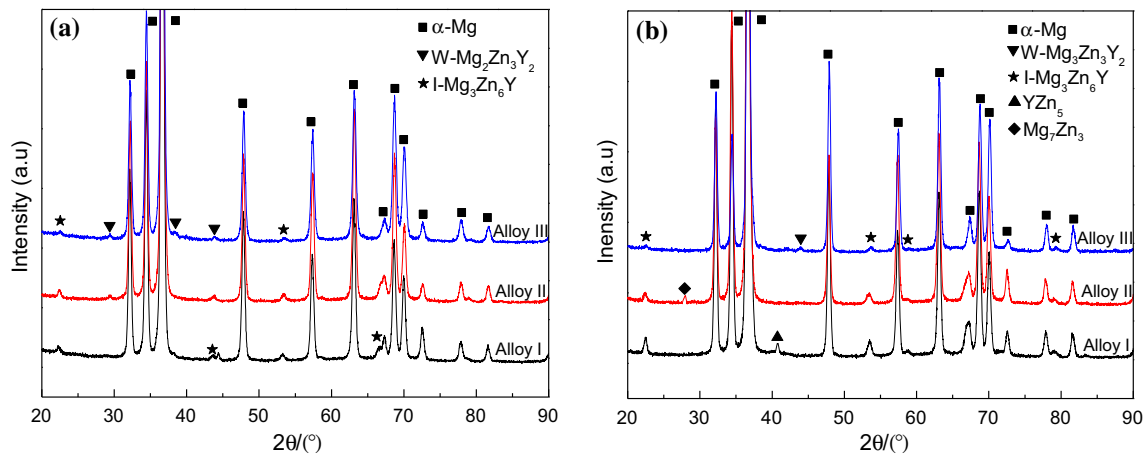
**Figure 3** Representative SEM microstructures of as-homogenized alloys: **a–c** low-magnification and **d–f** magnified images for the alloy (I–III), respectively.

micron-sized particles inside the grains mainly contain Mg and Zn elements and the mass ratio of Mg to Zn is close to 7:3, which preliminarily confirms the presence of  $Mg_7Zn_3$  (Fig. 3e). The undissolved  $Zn_3Zr_2$  phases are present in the alloys owing to their superior thermal stability (Fig. 3d–f). Similar phase composition is also determined from the XRD analysis (Fig. 4b). It is worth noting that the diffraction peaks from the I phase are remarkably strengthened in alloy I after the homogenization treatment.

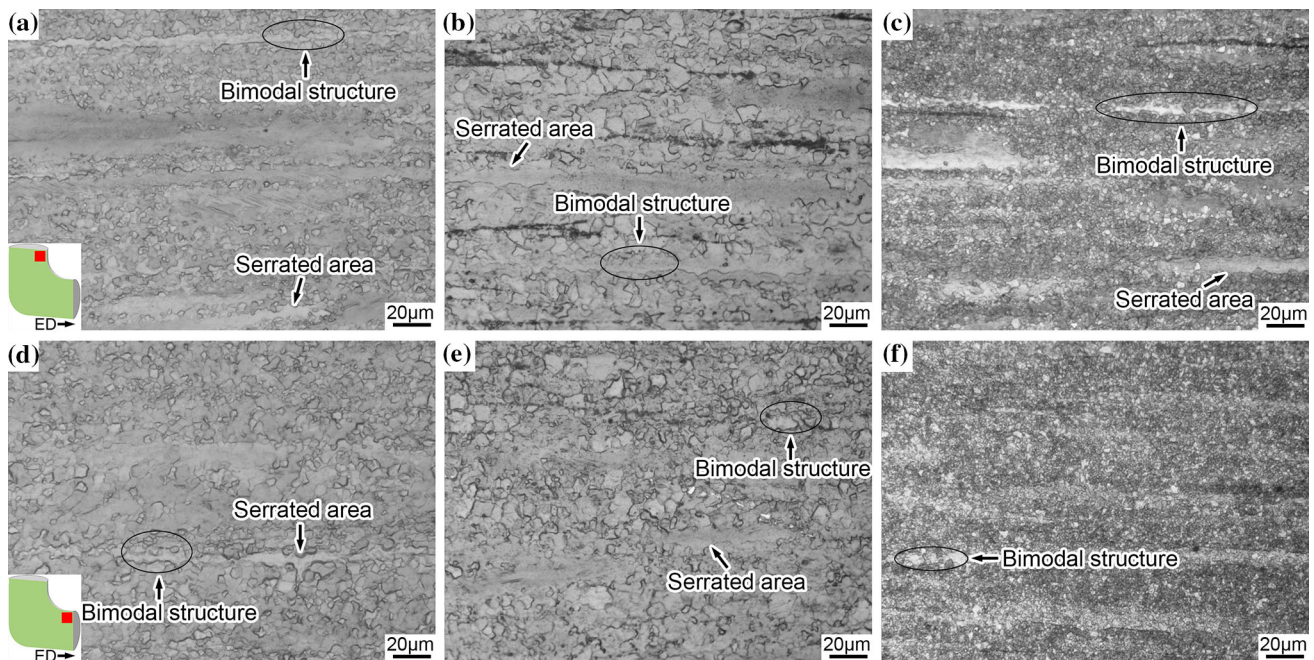
### Microstructural characteristics and texture evolution of ES alloys

Figure 5 shows the optical microstructures of the ES alloys in the extrusion and forming areas. A typical bimodal grain structure consisting of long serrated non-DRX areas and veined ultrafine DRX grains of alloys can be observed in the extrusion area and forming area. The area fraction or size of the non-DRX grains is gradually reduced with decreasing Zn/Y mass ratios, while obvious grain refinement is also observed as the Y content increased to 3 wt%. Similarly, this phenomenon also occurs in alloys in the forming area compared with the extrusion area. Therefore, excessive Y element and shear forces at the die corner play an important role on the DRX.

Figure 6 shows the SEM micrographs of the ES alloys in the forming area. The volume fractions of the undissolved particles obviously decrease with decreasing Zn/Y mass ratios. These particles are mainly distributed at the DRX area and along the ED because of the stronger PSN mechanism induced by the increased stress concentration during the ES process. The bulk particles with a size of  $\sim 2 \mu m$  are the I phases. The spherical-shaped particles composed of a fine extrusion streamline can be considered as the W phases after EDS analysis. The W phase with a poorer thermal stability is easily overcome during the ES process at  $400^\circ C$  [30]. Furthermore, the partial I and W phases are involved in the formation of a co-cluster (Fig. 6b, e). The fine particles at the grain boundaries and within the grain interior contain Y (3.65 at.%) and Zn (14.84 at.%), which are close to that of the  $YZn_5$  phase (Fig. 6a, d). The chemical composition of the finer particles aligned along the DRX grain boundaries is Mg-15.06 at.% and Zn-5.79 at.% with an atomic ratio close to 7:3 (Fig. 6e), and it can be recognized as the  $Mg_7Zn_3$  phase. In alloys I and II, the XRD pattern has the extra peaks of the  $YZn_5$  and  $Mg_7Zn_3$  phases, which is clearly observed in Fig. 7. The diffraction peaks of the W phase are markedly enhanced for alloys II and III in the forming area as compared with the extrusion



**Figure 4** XRD patterns of **a** as-cast and **b** as-homogenized alloys.

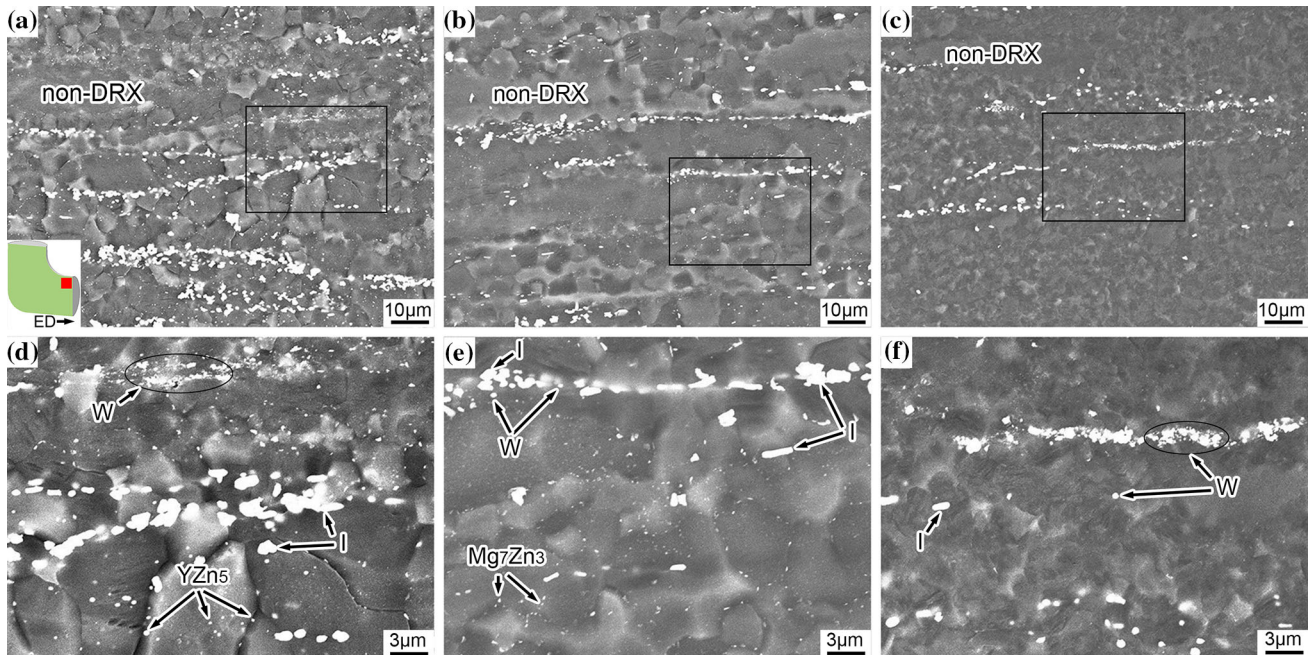


**Figure 5** Optical microstructures of the ES alloys: **a–c** images for the alloys (I–III) in extrusion area, respectively, and **d–f** images for the alloys (I–III) in forming area, respectively.

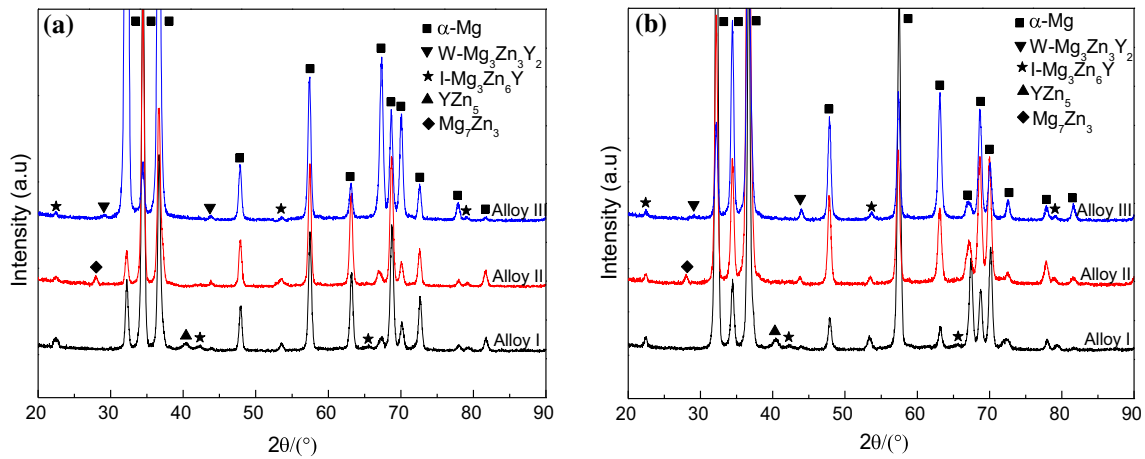
area, which indicates that a portion of the nano-sized W precipitates are present in the  $\alpha$ -Mg matrix but cannot be observed in the SEM images.

Figure 8 shows the EBSD results (perpendicular to the ED) for a comparative analysis of the inverse pole figure orientation maps (IPF-Y), (0002) pole figures, distributions of the misorientation angle, and the variations of the grain size of the ES alloys in the extrusion and forming areas. As the Zn/Y mass ratios decreased, the fractions of misorientation angles below  $5^\circ$  referred as the non-DRX grain boundaries decrease. Similar observations are also obtained from

the texture examination, where the reduced maximum intensities of the ED pole figures can be ascribed to the reinforced lattice distortion induced by the addition of more Y element that could act as a nucleation site for DRX during ES process [31]. Meanwhile, the fiber basal textures with basal planes of grains mostly parallel to the ED are weakened, and the typical basal textures with RE texture component can be clearly seen in alloy III (Fig. 8c, f). In addition, particularly for alloy I, the maximum intensities of the texture obviously decrease in the forming area compared with the extrusion area (Fig. 8a, d). This



**Figure 6** Representative SEM microstructures of the ES alloys: **a–c** low-magnification and **d–f** magnified images for the ES alloys (I–III), respectively.



**Figure 7** XRD patterns of the ES alloys in the **a** extrusion and **b** forming areas.

establishes that DRX is sensitive to the die corner, where the extra shear forces further facilitate DRX, except for alloy III (Fig. 8c, f). The mass of the dislocation recovers induced by the large amount of stored energy accounts for the unification of the fraction of misorientation angles below 5° and the maximum intensities of the texture utilized to estimate DRX. The average grain sizes of the ES alloys I, II, and III in the extrusion and forming areas are 2.60 μm, 3.00 μm, and 4.05 μm and 3.54 μm, 1.38 μm, and 1.59 μm, respectively. For alloys I and II (Fig. 8a, b, d, e), the reduced grain size is not positively

correlated with an increase in the Y element because more I phases are observed in alloy I. There is a high interfacial bonding energy between the I phase and the α-Mg matrix. This consequently results in a large amount of stress concentrations around them and a stronger PSN mechanism, which is in agreement with the published literature on the Mg–Zn–RE alloy system [32, 33]. Moreover, the variation in the average grain size during the ES process is related to the interaction between the growth of the fine DRX grains and recrystallization of the initial coarse non-DRX grains in the extrusion area [34]. Compared with

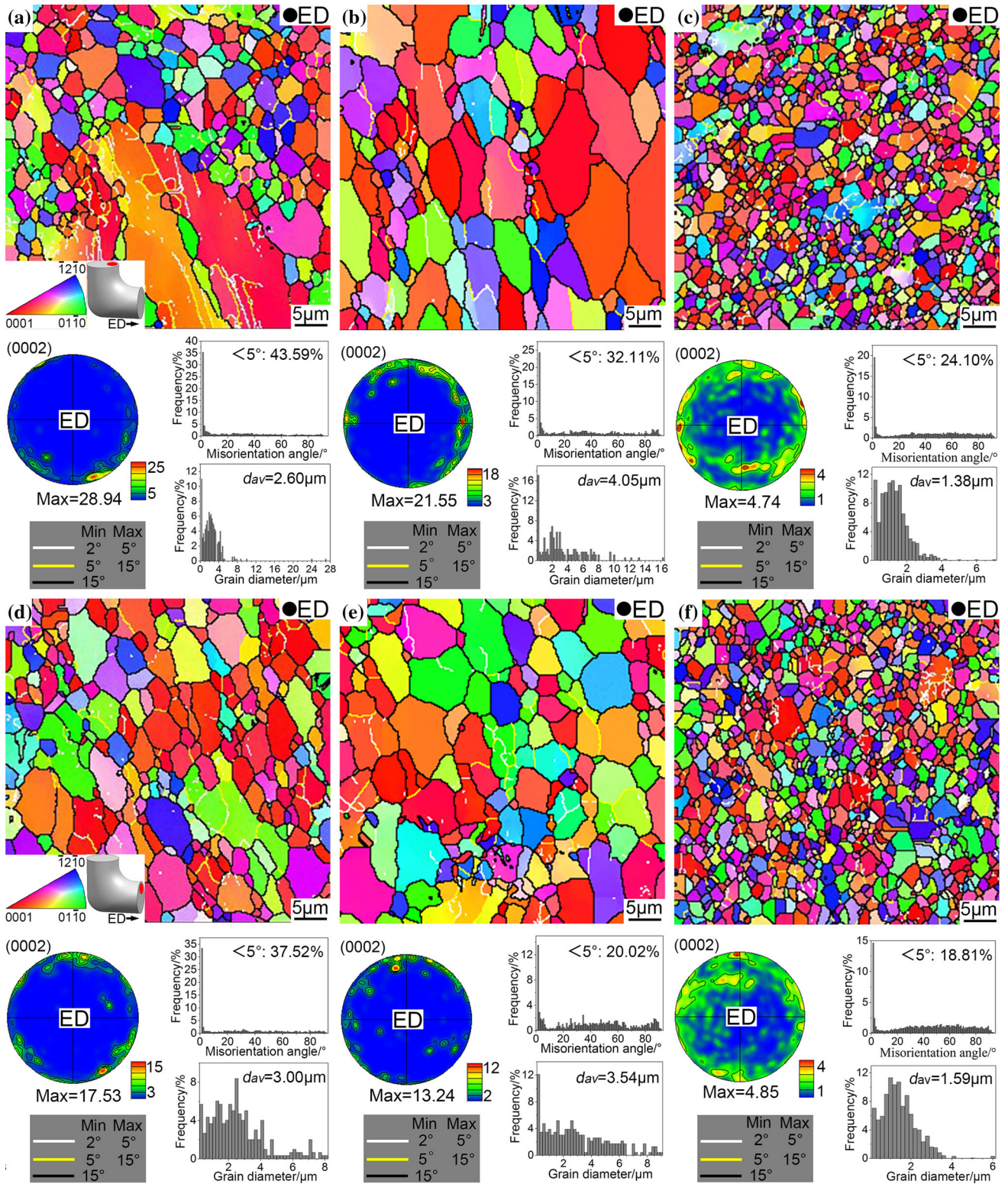


**Figure 8** EBSD results including IPF-Y, (0002) pole figure, distribution of misorientation angle, and distribution of grain size of the ES alloys: **a–c** images for the alloys (I–III) in the extrusion

area, respectively, and **d–f** images for the alloys (I–III) in the forming area, respectively.



the extrusion area, there is a slight increase in the average grain size, except for alloy II (Fig. 8b, e). This is ascribed to the stronger grain-boundary pinning effect induced by the substantial amount of micro-sized  $Mg_7Zn_3$  phases. Interestingly, the extent of the fine DRX grain growth in alloy III is less than that of alloy I, in spite of the abundant fine spherical-shaped  $YZn_5$  phases observed at the DRX grain boundaries in alloy I (Fig. 6a, d).

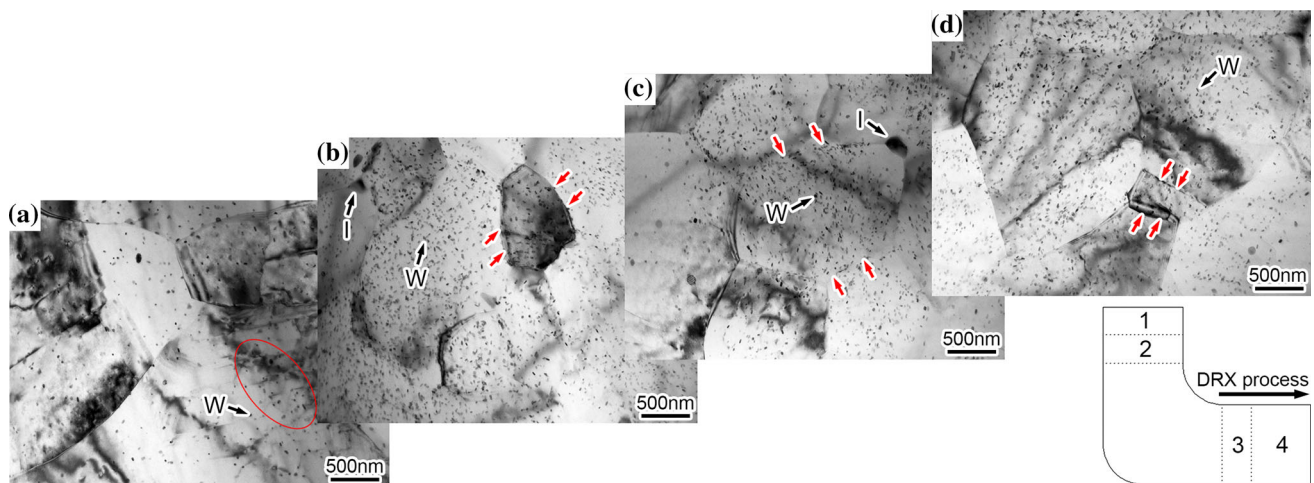
Figure 9 shows the TEM images of the microstructures of ES alloy III from four different regions. The fine W precipitates with a size of 20–40 nm are present not only within the DRX grains interior but also at the DRX boundaries (Fig. 9a–d). The bulk I phases with a size of 200–250 nm are aligned along the DRX boundaries (Fig. 9b, c). The W precipitate interferes with the motion of dislocations, which in turn facilitates the dislocation pileups and tangles that can aggravate dynamic precipitation [35]. The abundant W precipitates act as barriers to dislocation movement, resulting in an increased intensity of dislocations and the emergence of sub-boundaries, as indicated by the red ellipses in Fig. 9a. The accumulated recovery of dislocations within the DRX grains by dislocation climbing contributes to the DRX behavior, because the extrusion experiment is carried out at an elevated extrusion temperature of 400 °C [36]. The sub-boundaries eventually evolve into fine DRX grains with a size of 500 nm, as indicated by the red arrow in Fig. 9b. The actual temperature increases by ~ 50 °C near the die corner under the joint action of deformation heat and friction heat generated during ES process [37]. Hence,

although the sparse W precipitates act as effective pinning obstacles against fine DRX grain growth, the excessive temperature markedly weakens the pinning effect. This results in the growth of fresh DRX grains to some extent, as indicated by the red arrow in Fig. 9c. The bulging of the parent grain boundaries is responsible for the formation of a fresh sub-grain structure at an adequate strain rate and severe lattice strain, as indicated by the red arrow in Fig. 9d. This phenomenon is termed as a continuous DRX; therefore, the uniform and fine equiaxial grain structure observed in the ES alloy III in the forming area is reasonable.

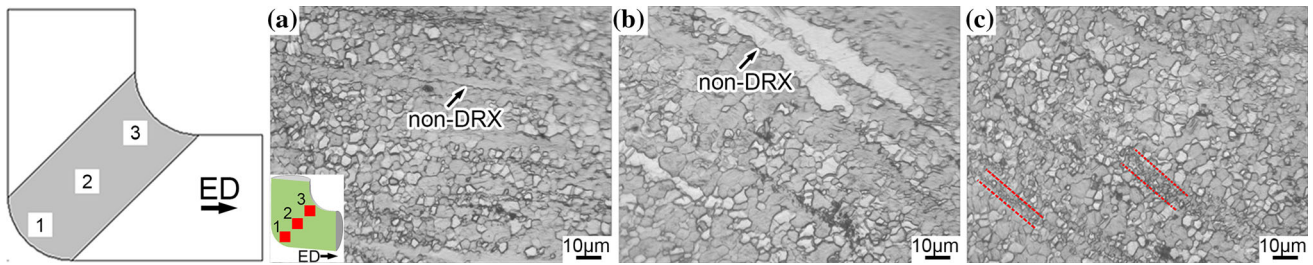
### Microstructural characteristics and texture evolution of alloys at the die corner during the ES process

Figure 10 shows the optical micrographs of the ES alloy I at the die corner. The typical bimodal microstructure is present at region 1, while coarser non-DRX grains are present at region 2. However, in region 3, coarse non-DRX grains are not observed, while the extruded streamlines composed of ultrafine DRX grains are visible as highlighted by the red dotted line in Fig. 10c. This demonstrates the diverse influences of the different regions at the die corner on DRX.

To clarify the influence of the extra shearing forces at the die corner on DRX, EBSD (parallel to the ED) on the die corner of the ES alloy I is taken, as shown in Fig. 11. From regions 1–3, the corresponding fractions of misorientation angles below 5° are 22.56%,



**Figure 9** Representative TEM microstructures of the ES alloy III: a–d images for regions (1–4), respectively.



**Figure 10** Optical microstructures of alloy I in the die corner: **a–c** images for regions (1–3), respectively.

42.79%, and 39.09%, respectively, while the maximum pole intensities are 12.95, 35.08, and 17.98, respectively. Considering the fraction of misorientation angles below  $5^\circ$  and the maximum pole density as mentioned in “Microstructural characteristics and texture evolution of ES alloys,” the external shearing angle (region 1) exhibits a more complete DRX structure than the other two regions (referred to as region 2 and 3). Similarly, the pronounced complete DRX has a convex-shaped tendency from region 1 to 3. The average grain sizes are  $2.37\ \mu\text{m}$  (region 1),  $3.32\ \mu\text{m}$  (region 2), and  $2.61\ \mu\text{m}$  (region 3), respectively. The grain diameter distribution is

concentrated at  $\sim 2.5\ \mu\text{m}$  in region 1, which also illustrates the maturation of the DRX from another viewpoint. The elongated non-DRX grains have massive sub-grain boundaries and small-angle grain boundaries, which confirms that the principal role of the die corner is the stimulation of further DRX. The  $\{01\bar{1}0\}$  plane of the most of fine DRX grains composed of extrusion streamlines approximately parallels to the ED, as indicated by the black ellipses in Fig. 11a. The  $\{10\bar{1}2\}$  extension twinning can reorient the basal plane of the parent grains by  $86^\circ$  [38]. Hence, it can be inferred that these DRX grains may be the evolution of the  $\{10\bar{1}2\}$  extension twinning. Besides, a striking

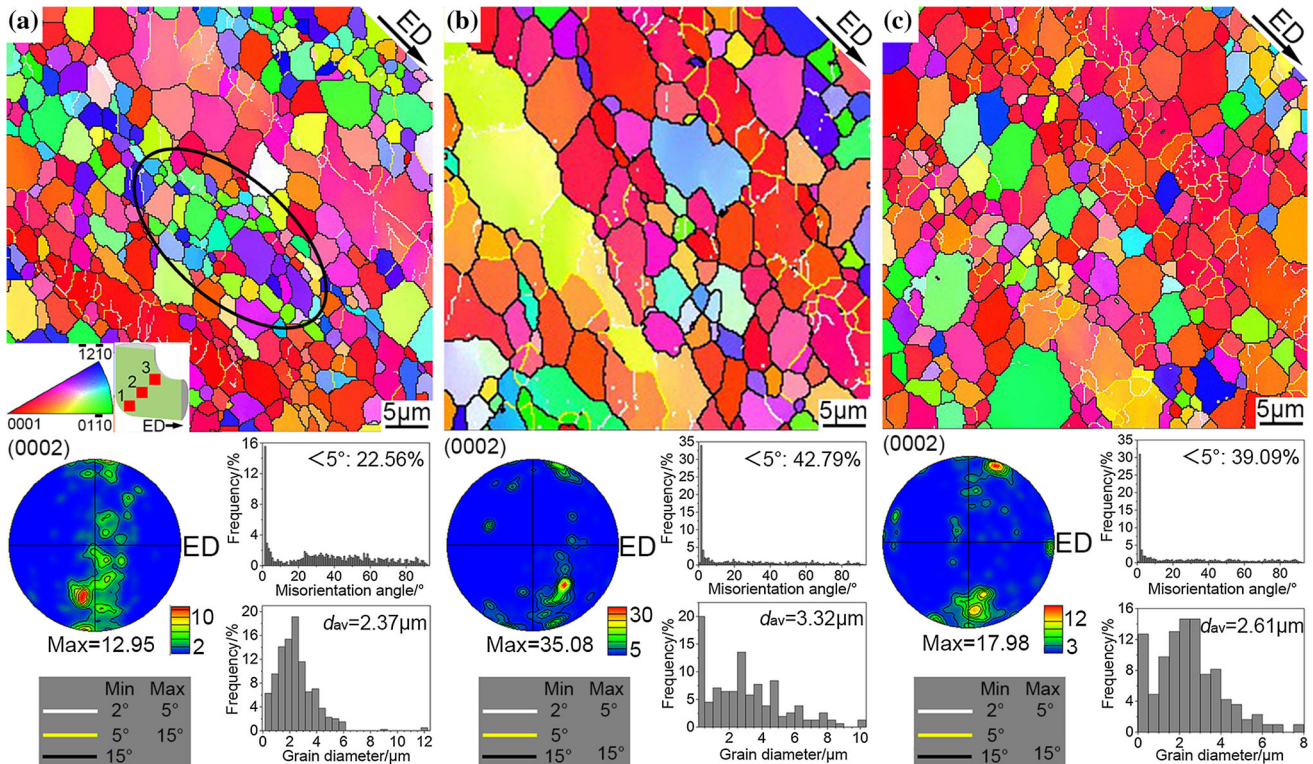


**Figure 11** EBSD results including IPF-Y, (0002) pole figure, distribution of misorientation angle, and distribution of grain size of the ES alloys I in the die corner: **a–c** images for the external

rotation angle (region 1), corner center (region 2), and internal rotation angle (region 3), respectively.

feature is that the three regions have basal poles tilting away from the ED by  $10^{\circ}$ – $20^{\circ}$ .

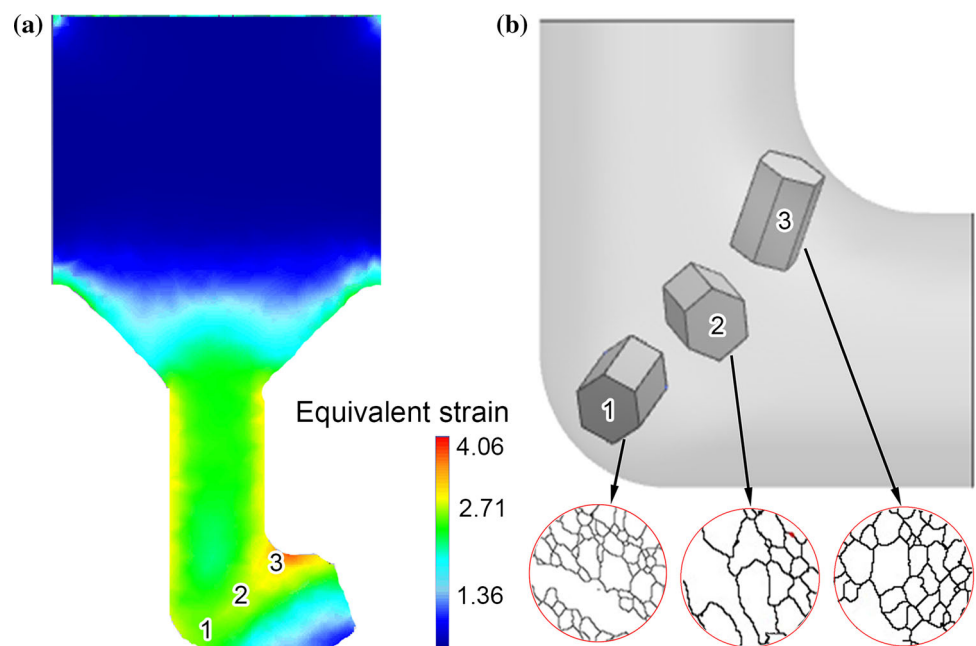
The complementary simulations for the equivalent strain during the ES process were carried out using the DEFORMT M-3D software to evaluate the microstructural evolution at the die corner, as shown in Fig. 12. The equivalent strains of regions 1, 2, and 3 are referred to  $\varepsilon_1$ ,  $\varepsilon_2$ , and  $\varepsilon_3$ , respectively, where  $\varepsilon_1 \approx \varepsilon_2 < \varepsilon_3$  (Fig. 12a). The equivalent strain accounts for the distribution of the microstructures in the Mg alloys during the ES process, where a larger strain results in a higher temperature [39]. The contributions of elevated temperature to the high DRX fraction and the growth of fine DRX grains have been demonstrated in the previous literature [40]. So, the presence of a fully DRX structure for samples in region 3 is not accidental (Fig. 12b). The microstructures of alloy I in regions 1 and 2 should be similar for approximately equivalent strains at the die corner, but this is not observed. This further confirms that a novel DRX is present in region 1, as mentioned above.

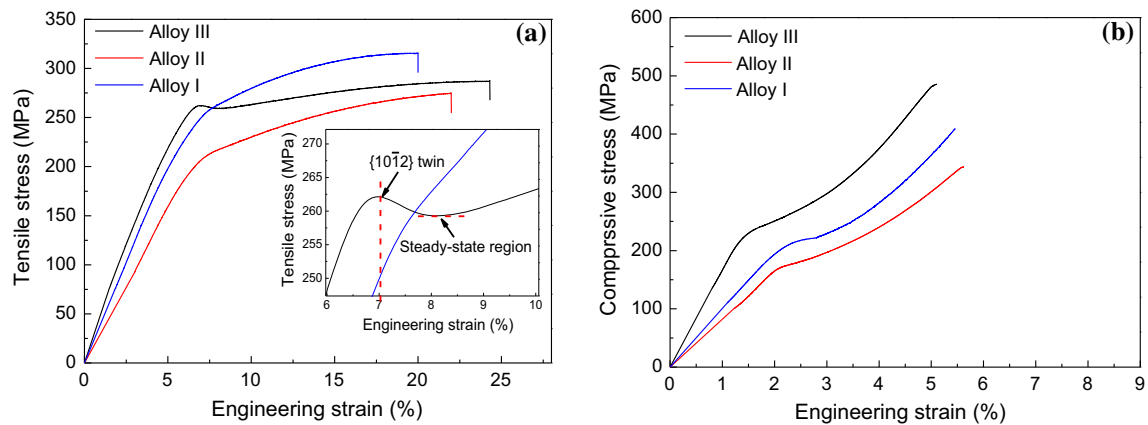
### Mechanical properties of ES alloys

Figure 13 shows the tensile and compressive stress–strain curves of the ES alloys in the forming area, and the corresponding values including the ultimate tensile strength (UTS), tensile yield strength (TYS), compressive yield strength (CYS), elongation to

failure ( $\delta$ ), and CYS/TYS are listed in Table 2. With decreasing Zn/Y mass ratios, the tensile strength, except for the TYS of alloy III, and yield asymmetry decrease gradually with significantly improved ductility. The improved tensile strength of the extruded Mg alloys is mainly dependent on the reduced grain size and strong texture-hardening effect under tensile loading parallel to ED. In this study, the ES alloy I exhibits better tensile strength (UTS of 316 MPa and TYS of 245 MPa) with a higher yield asymmetry (CYS/TYS of 0.80) than that of the ES alloy II. This can be ascribed to the finer average grain size of  $3.00 \mu\text{m}$  and the stronger basal texture. The ES alloy III displays an excellent tensile strength–ductility combination (TYS of 262 MPa and elongation of 24%) because of having the finest DRX grains of  $1.59 \mu\text{m}$ , substantial W phases with superior ductility, and a weakened basal texture with an RE texture component. Normally, the basal slip and  $\{10\bar{1}2\}$  extension twin with a low CRSS are the dominant deformation mechanisms in the extruded Mg alloys under tensile loading along the ED at ambient temperature [41]. An evident concave-shaped curve is obtained when the engineering strain reaches  $\sim 7\%$  of the ES alloy III, which is closely related to the activation of the  $\{10\bar{1}2\}$  extension by increasing the Schmid factor. Koike et al. [42] also indicated that the presence of the steady-state region in the tensile stress–strain curves contributed to an increase in the intensity of mobile dislocations. This was due to the activation of the

**Figure 12** **a** Schematic diagram of the equivalent strain obtained using the DEFORMT M-3D software and **b** preferred orientation and evolution of the DRX grain at the die corner.





**Figure 13** a Tensile and b compressive stress–strain curves of ES alloys.

**Table 2** Tensile and compression test results of the ES alloys

Samples	UTS (MPa)	TYS (MPa)	CYS (MPa)	$\delta$ (%)	CYS/TYS
Alloy I	316	245	195	20	0.80
Alloy II	278	197	167	22	0.85
Alloy III	287	264	224	24	0.92

basal slip systems near the grain boundaries and a large quantity of precipitates, which in turn deteriorated the UTS of the alloy.

## Conclusions

The microstructure, mechanical properties, and texture evolution of the as-cast, as-homogenized, and ES Mg–Zn–Y–Zr alloys with Zn/Y mass ratios of 4, 1.5, and 0.67 were systematically investigated. The major conclusions can be summarized as follows:

1. The as-cast alloys were mainly composed of  $\alpha$ -Mg matrix, W, and I phases. As the mass ratio of Zn/Y decreased, the I phase dominated the phase composition. Moreover, the LPSO phase could not be observed in alloy III.
2. After a long homogenization treatment, the W phase dissolved in the  $\alpha$ -Mg matrix but not in the I phase. Interestingly, the needle-shaped  $\text{YZn}_5$  and micro-sized  $\text{M}_7\text{Zn}_3$  phases were also observed in alloys I and II.
3. The equivalent strain and higher temperatures in the die corner induced further DRX and a slight growth of the fine DRX grains, and the basal fiber texture was weakened. The uneven distribution of the equivalent strain was responsible for the

different microstructures and textures at the die corner.

4. The interactions between mechanical properties and the grain size, basal texture, and phases were comprehensively investigated. Here, the ES alloy III had an excellent tensile strength–ductility combination because it had the finest DRX grains, substantial W phases, and a weakened basal texture with RE texture component.

## Acknowledgements

This research was supported by “Xingliao Elite” Project of Liaoning Province (XLYC1807021), Youth Project of Liaoning Education Department (LQGD2017032), National Natural Science Foundation (51504153), and Innovation Talent Program in Sciences and Technologies for Young and Middle-aged Scientists of Shenyang (RC180111).

## Compliance with ethical standards

**Conflict of interest** The authors declare that they have no conflict of interest.

## References

- [1] Kulekci MK (2008) Magnesium and its alloys applications in automotive industry. *Int J Adv Manuf Technol* 39:851–865
- [2] Mordike BL, Ebert T (2001) Magnesium properties–applications–potential. *Mater Sci Eng, A* 302(1):37–45
- [3] Yuan W, Panigrahi SK, Su J-Q, Mishra RS (2011) Influence of grain size and texture on Hall–Petch relationship for a magnesium alloy. *Scr Mater* 65(11):994–997
- [4] Song B, Xin RL, Chen G, Zhang XY, Liu Q (2012) Improving tensile and compressive properties of magnesium alloy plates by pre-cold rolling. *Scr Mater* 66(12):1061–1064
- [5] Krajčák T, Minárik P, Stráská J, Gubicza J, Máthi K, Milos J (2019) Influence of the initial state on the microstructure and mechanical properties of AX41 alloy processed by ECAP. *J Mater Sci* 54(4):3469–3484. <https://doi.org/10.1007/s10853-018-3033-6>
- [6] Chino Y, Kimura K, Mabuchi M (2008) Twinning behavior and deformation mechanisms of extruded AZ31 Mg alloy. *Mater Sci Eng, A* 486(1–2):481–488
- [7] Wang MY, Xin RL, Wang BS, Liu Q (2011) Effect of initial texture on dynamic recrystallization of AZ31 Mg alloy during hot rolling. *Mater Sci Eng, A* 528(6):2941–2951
- [8] Luo AA, Mishra RK, Sachdev AK (2011) High-ductility magnesium–zinc–cerium extrusion alloys. *Scr Mater* 64(5):410–413
- [9] Janeček M, Yi S, Král R, VrátnáJ Kainer KU (2010) Texture and microstructure evolution in ultrafine-grained AZ31 processed by EX-ECAP. *J Mater Sci* 45(17):4665–4671. <https://doi.org/10.1007/s10853-010-4675-1>
- [10] Figueiredo RB, Langdon TG (2006) The development of superplastic ductilities and microstructural homogeneity in a magnesium ZK60 alloy processed by ECAP. *Mater Sci Eng, A* 430(1–2):151–156
- [11] Imandoust A, Barrett CD, Al-Samman T, Inal KA, El Kadiriet H (2017) A review on the effect of rare-earth elements on texture evolution during processing of magnesium alloys. *J Mater Sci* 52(1):1–29. <https://doi.org/10.1007/s10853-016-0371-0>
- [12] Xu C, Nakata T, Fan GH, Li XW, Tang GZ, Geng L, Kamado S (2019) Microstructure and mechanical properties of extruded Mg–Gd–Y–Zn alloy with Mn or Zr addition. *J Mater Sci* 54:10473–10488. <https://doi.org/10.1007/s10853-019-03607-4>
- [13] Sanjari M, Kabir ASH, Farzadfar A, Ustunomiya H, Petrov R, Kestens L, Yue S (2014) Promotion of texture weakening in magnesium by alloying and thermomechanical processing: (I) alloying. *J Mater Sci* 49(3):1408–1425. <https://doi.org/10.1007/s10853-013-7826-3>
- [14] Sanjari M, Farkoosh AR, Shalchi Amirkhiz B, He Y, Javaid A, Kabir AS, Su J, Jung IH, Yue S (2017) The role of the Zn/Nd ratio in the microstructural evolution of the Mg–Zn–Nd system during static recrystallization: grain boundary partitioning of solutes. *Scr Mater* 134:1–5
- [15] Zhang JS, Chao X, Cheng WL, Bian LP, Wang HG, Xu CX (2013) Research on long-period-stacking-ordered phase in Mg–Zn–Dy–Zr alloy. *J Alloys Compd* 558(5):195–202
- [16] Kim S-H, Lee JU, Kim YJ, Jung J-G, Park SH (2018) Controlling the microstructure and improving the tensile properties of extruded Mg–Sn–Zn alloy through Al addition. *J Alloys Compd* 751:1–11
- [17] Lee JY, Kim DH, Lim HK, Kim DH (2005) Effects of Zn/Y ratio on microstructure and mechanical properties of Mg–Zn–Y alloys. *Mater Lett* 59(29–30):3801–3805
- [18] Shen MJ, Wang XJ, Li CD, Zhang MF, Hu XS, Zheng MY, Wu K (2013) Effect of bimodal size SiC particulates on microstructure and mechanical properties of AZ31B magnesium matrix composites. *Mater Des* 52:1011–1017
- [19] Park SS, Kim YJ, Cheng WL, Kim YM (2011) Tensile properties of extruded Mg–8Sn–1Zn alloys subjected to different heat treatments. *Philos Mag Lett* 91(1):35–42
- [20] Yin SQ, Zhang ZQ, Liu X, Le QC, Lan Q, Bao L, Cui JZ (2017) Effects of Zn/Gd ratio on the microstructures and mechanical properties of Mg–Zn–Gd–Zr alloys. *Mater Sci Eng, A* 695:135–143
- [21] Xu DK, Liu L, Xu YB, Han EH (2007) Effect of microstructure and texture on the mechanical properties of the as-extruded Mg–Zn–Y–Zr alloys. *Mater Sci Eng, A* 443(1–2):248–256
- [22] Jiang MG, Xu C, Nakata T, Yan H, Chen RS, Kamado S (2016) Development of dilute Mg–Zn–Ca–Mn alloy with high performance via extrusion. *J Alloy Compd* 668:13–21
- [23] Oh-ishi K, Mendis CL, Homma T, Kamado S, Ohkubo T, Hono K (2009) Bimodally grained microstructure development during hot extrusion of Mg–2.4Zn–0.1Ag–0.1Ca–0.16Zr(at.%) alloys. *Acta Mater* 57(18):5593–5604
- [24] Bai Y, Cheng WL, Ma SC, Zhang J, Guo C, Zhang Y (2018) The influence of initial microstructure on the strengthening effect of extruded Mg–8Sn–4Zn–2Al alloys. *Acta Metall Sin* 31(5):487–495
- [25] Zhang DF, Hu H-J, Pan FS, Yang MB, Zhang JP (2010) Numerical and physical simulation of new SPD method combining extrusion and equal channel angular pressing for AZ31 magnesium alloy. *Trans Nonferr Metal Soc* 20(3):478–483
- [26] Dumitru F-D, Higuera-Cobos OF, Cabrera JM (2014) ZK60 alloy processed by ECAP: microstructural, physical and mechanical characterization. *Mater Sci Eng, A* 594:32–39

- [27] Geng JW, Teng XY, Zhou GR, Zhao DG (2013) Microstructure transformations in the heat-treated Mg–Zn–Y alloy. *J Alloy Compd* 577:498–506
- [28] Li JC, He ZL, Fu PH, Wu YJ, Peng LM, Ding WJ (2016) Heat treatment and mechanical properties of a high-strength cast Mg–Gd–Zn alloy. *Mater Sci Eng, A* 651:745–752
- [29] Xu DK, Tang WN, Liu L, Xu YB, Han EH (2007) Effect of Y concentration on the microstructure and mechanical properties of as-cast Mg–Zn–Y–Zr alloys. *J Alloy Compd* 432(1–2):129–134
- [30] Singh A, Watanabe M, Kato A, Tsai AP (2004) Microstructure and strength of quasicrystal containing extruded Mg–Zn–Y alloys for elevated temperature application. *Mater Sci Eng, A* 385(1–2):382–396
- [31] Xu SW, Zheng MY, Kamado S, Wu K (2012) The microstructural evolution and superplastic behavior at low temperatures of Mg–5.00Zn–0.92Y–0.16Zr (wt%) alloys after hot extrusion and ECAP process. *Mater Sci Eng, A* 549:60–68
- [32] Bohlen J, Yi SB, Letzig D, Kainer KU (2010) Effect of rare earth elements on the microstructure and texture development in magnesium-manganese alloys during extrusion. *Mater Sci Eng, A* 527(26):7092–7098
- [33] Huppmann M, Gall S, Müller S, Reimers W (2010) Changes of the texture and the mechanical properties of the extruded Mg alloy ME21 as a function of the process parameters. *Mater Sci Eng, A* 528(1):342–354
- [34] Chen HB, Liu TM, Zhang Y, Song B, Hou DW, Pan FS (2016) The yield asymmetry and precipitation behavior of pre-twinned ZK60 alloy. *Mater Sci Eng, A* 652:167–174
- [35] Wang XJ, Wu K, Zhang HF, Huang WX, Chang H, Gan WM, Zheng MY, Peng DL (2007) Effect of hot extrusion on the microstructure of a particulate reinforced magnesium matrix composite. *Mater Sci Eng, A* 465(1–2):78–84
- [36] Xu SW, Zheng MY, Kamado S, Wu K, Wang JG, Lv XY (2011) Dynamic microstructural changes during hot extrusion and mechanical properties of a Mg–5.0Zn–0.9Y–0.16Zr (wt%) alloy. *Mater Sci Eng, A* 528(12):4055–4067
- [37] Jung J-G, Park SH, You BS (2015) Effect of aging prior to extrusion on the microstructure and mechanical properties of Mg–7Sn–1Al–1Zn alloy. *J Alloys Compd* 627:324–332
- [38] Xin YC, Wang MY, Zeng Z, Huang GJ, Liu Q (2011) Tailoring the texture of magnesium alloy by twinning deformation to improve the rolling capability. *Scr Mater* 64(10):986–989
- [39] Figueiredo RB, Cetlin PR, Langdon TG (2007) The processing of difficult-to-work alloys by ECAP with an emphasis on magnesium alloys. *Acta Mater* 55(14):4769–4779
- [40] Wusatowska-Sarneck AM, Miura H, Sakai T (2002) Nucleation and microtexture development under dynamic recrystallization of copper. *Mater Sci Eng, A* 323(1–2):177–186
- [41] Jiang L, Jonas JJ, Mishra RK, Luo A, Sachdev AK, Godet S (2007) Twinning and texture development in two Mg alloys subjected to loading along three different strain paths. *Acta Mater* 55(11):3899–3910
- [42] Koike J, Kobayashi T, Mukai T, Watanabe H, Suzuki M, Maruyama K, Higashi K (2003) The activity of non-basal slip systems and dynamic recovery at room temperature in fine-grained AZ31B magnesium alloys. *Acta Mater* 51(7):2055–2065

**Publisher's Note** Springer Nature remains neutral with regard to jurisdictional claims in published maps and institutional affiliations.